Mineralogia, vol. 55, 2024, 48-59 *Original Paper*

DOI: 10.2478/mipo-2024-0005

Mimetite and polymineralic mimetite-pyromorphite-vanadinite single crystals from the Sowie Mts, Poland

Eligiusz Szełęg[1,*], Janusz Janeczek[1], Rafał Juroszek[1], Marta Danila[2]

[1]Institute of Earth Sciences, University of Silesia in Katowice, Będzińska 60, 41-200 Sosnowiec, Poland;
[2]Schlesienstraße 15, 63110 Rodgau, Germany

*Corresponding author: eligiusz.szeleg@us.edu.pl

Abstract

Millimeter-sized crystals of mimetite and pyromorphite, and polymineralic mimetite-pyromorphite-vanadinite crystals occur in quartz-baryte vein within paragneisses of the Sowie Mts, SW Poland. Three morphologically different mimetite crystals and a polymineralic crystal were examined by electron probe micro-analysis (EPMA), back-scattered electrons (BSE) imaging, Raman microspectroscopy, and X-ray composition mapping. Mimetite occurs as well-developed crystals, crystals built up of sub-parallel individuals due to autoepitaxial growth, and crystals extensively etched. All of the mimetite crystals are zoned with respect to pyromorphite molecule content with sharp increase up to 23 mol% in the outermost zones. The apparent vanadinite crystal actually consists of oscillatory-zoned pyromorphite + minor vanadinite core, intermediate zones composed of pyromorphite, two mimetite zones intercalated by a band of oscillatory pyromorphite and minor vanadinite, and vanadinite mantle. EPMA data show a limited miscibility between all three minerals in the polymineralic crystal. Most analyzes cluster around 10 mol% of ternary solid solution with the maximum value of ca. 30 mol%. X-ray elemental maps reveal sharp boundaries between compositionally contrasting zones in the crystal core. In mimetite zones, the substitution of As by P does not exceed 0.43 atoms per formula unit (apfu). In the vanadinite mantle, As + P does not exceed 0.30 apfu. The distribution of Pb is uniform throughout the crystal with the highest Ca/Pb ratio of 0.03. The observed sequence of crystallization in the polymineralic crystal can be explained by the relative changes in ions concentrations at the crystal/solution interface, i.e. within the diffusion boundary layer, in accord with the models of the autocatalytic crystal growth. The authors hypothesize that kinetically driven fast growth of the polymineralic crystals resulted in precipitation of discrete mineral phases with very limited anionic substitutions.

Keywords: mimetite, pyromorphite, vanadinite, crystal overgrowths, compositional zoning

1. Introduction

Lead-bearing members of the apatite supergroup collectively termed Pyromorphite Group Minerals (PyGM): mimetite, $Pb_5(AsO_4)_3Cl$, pyromorphite, $Pb_5(PO_4)_3Cl$, and vanadinite, $Pb_5(VO_4)_3Cl$, often form anion solid solutions (Pasero et al., 2010). In addition to anionic substitutions, Ca may proxy for Pb in small

amounts (usually <1 wt%). The complete anionic solid solution between mimetite and pyromorphite [$Pb_5(AsO_4)_{3-x}(PO_4)_xCl$] has been well documented through mineralogical studies (Markl et al., 2014 and references therein) and experimentally (Inegbenebor et al., 1989; Flis et al., 2011). According to Markl et al. (2014) the asymmetrical solvus exists between vanadinite and pyromorphite with the highest recorded value of 39 mol% pyromorphite component in vanadinite. However, spectroscopic and experimental studies showed a complete and continuous solid solution between pyromorphite and vanadinite and between mimetite and vanadinite (Frost et al., 2003; Solecka et al., 2018; Song et al., 2018; Puzio et al., 2021). Solid solutions between pyromorphite and vanadinite, and between mimetite and vanadinite depend on pH; whereas, T is of less importance (Janicka et al., 2014).

Pyromorphite group minerals commonly show compositional zoning in respect to anions and Ca/Pb. Mutual overgrowths of those minerals have been observed in various configurations, i.e. pyromorphite overgrowing vanadinite and vice versa (Markl et al., 2014), and pyromorphite overgrowing mimetite (Nakamoto et al., 1969; Kepper, 2004).

In this paper we report the occurrence of mimetite and apparently single crystals of vanadinite from the quartz-baryte vein in paragneisses of the Sowie Mts, SW Poland. The apparent vanadinite crystals are actually composed of multiple zones and overgrowths of pyromorphite, mimetite, and vanadinite. To our knowledge, such a complex pattern of zoning and overgrowths in PyGM has not yet been reported.

Unlike pyromorphite and mimetite, which are known from numerous Pb-bearing ore deposits in Poland (Szełęg, 2023), vanadinite was reported only from the single locality in the abandoned quartz mine in the Izera Mts (Szełęg, 2008).

2. Samples and Methods

2.1. Study area and sample description

A few apparent vanadinite crystals together with crystals of pyromorphite and mimetite were collected from dumps at the abandoned "Friedrich von Thielau" galena and baryte mine near the village Grodziszcze (former Lampersdorf) (50°37'32" N 16°39'16" E) in the Sowie Mts, SW Poland. The quartz-baryte vein, ca. 120 m long and up to 1.5 m thick was exploited for argentiferous galena in the 19th century and for baryte at the beginning of the 20th century (Stysz & Mączka, 2007). Hydrothermal quartz-baryte veins are hosted by biotite-oligoclase paragneisses and migmatites dated at 385-360 Ma (Breemen et al., 1988; Jastrzębski et al., 2021).

Galena crystals up to 2 cm in size occur sparsely in the vein with no physical contact with the secondary Pb minerals. Mimetite is the most abundant secondary Pb-mineral in the collected samples. Mimetite from Grodziszcze was first observed by Traube (1888) as yellow-greyish barrel-shaped crystals on galena. Mimetite occurs as single crystals (Fig. 1) or radial aggregates of crystals. Pyromorphite pale-green acicular crystals, up to 0.5 mm long, occur on platy baryte crystals either as radial aggregates or bundles of crystals (Fig. 2).

Spindle-shaped grey to dark brown crystals composed of subparallel individuals split at their terminations (Fig. 3), up to 4 mm long, with adamantine luster occur on baryte in association with cerussite. X-ray energy-dispersive (EDX) spectra of those crystals show their chemical composition typical of vanadinite. However, inspection of the crystals interiors revealed their polymineralic nature with multiple zoning and overgrowths of mimetite, pyromorphite, and vanadinite. The crystals are brittle and easy to crumble. Due to technical problems with sample preparation only one of those crystals was suitable for the detailed examination.

2.2. Methods

Samples were investigated by optical microscopy, scanning electron microscopy (SEM), electron probe microanalysis (EPMA), and Raman microspectroscopy. Mineral morphology and spatial distribution of relevant elements within observed minerals were examined using a Philips XL 30 ESEM/TMP scanning electron microscope coupled to an energy-dispersive spectrometer (EDAX type Sapphire) at the Institute of Earth Sciences, University of Silesia. Operating conditions were: accelerating voltage 15 kV; working distance ca. 10 mm; counting time 40 s. The same conditions were applied for back-scattered electron (BSE) imaging.

Chemical compositions of minerals were determined using a CAMECA SX-100 microprobe at the Laboratory of Electron Microscopy, Microanalysis and X-ray Diffraction at the University of Warsaw Faculty of Geology, Warsaw, Poland. The microprobe operated in the wavelength-dispersive (WDS) mode at an accelerating voltage of 15 kV and a beam current of 10 nA. Counting time for each element was 40 s at the peak position and 20 s for background. The electron beam diameter was 5 µm. *L*α lines were measured for As, Cd, Pb and *M*α lines for Bi. *K*α lines were measured for other elements. The following standards were used: GaAs for As; YPO_4 for P; V_2O_5 for V; sphalerite for Zn, crocoite for Pb, Bi_2Te_3 for Bi; diopside for Si and Ca, hematite for Fe. The number of atoms in a formula unit (apfu) were calculated from the obtained EPMA data expressed in weight percent (wt%) based on 12.5 oxygen equivalents as recommended by Ketcham (2015).

Raman spectra of vanadinite and mimetite were recorded with the WITec alpha 300R Confocal Raman Microscope (Institute of Earth Sciences, Faculty of Natural Sciences, University of Silesia, Sosnowiec, Poland) equipped with an air-cooled solid laser 532 nm and a CCD camera operating at -61°C. The laser radiation was coupled to a microscope through a single-mode

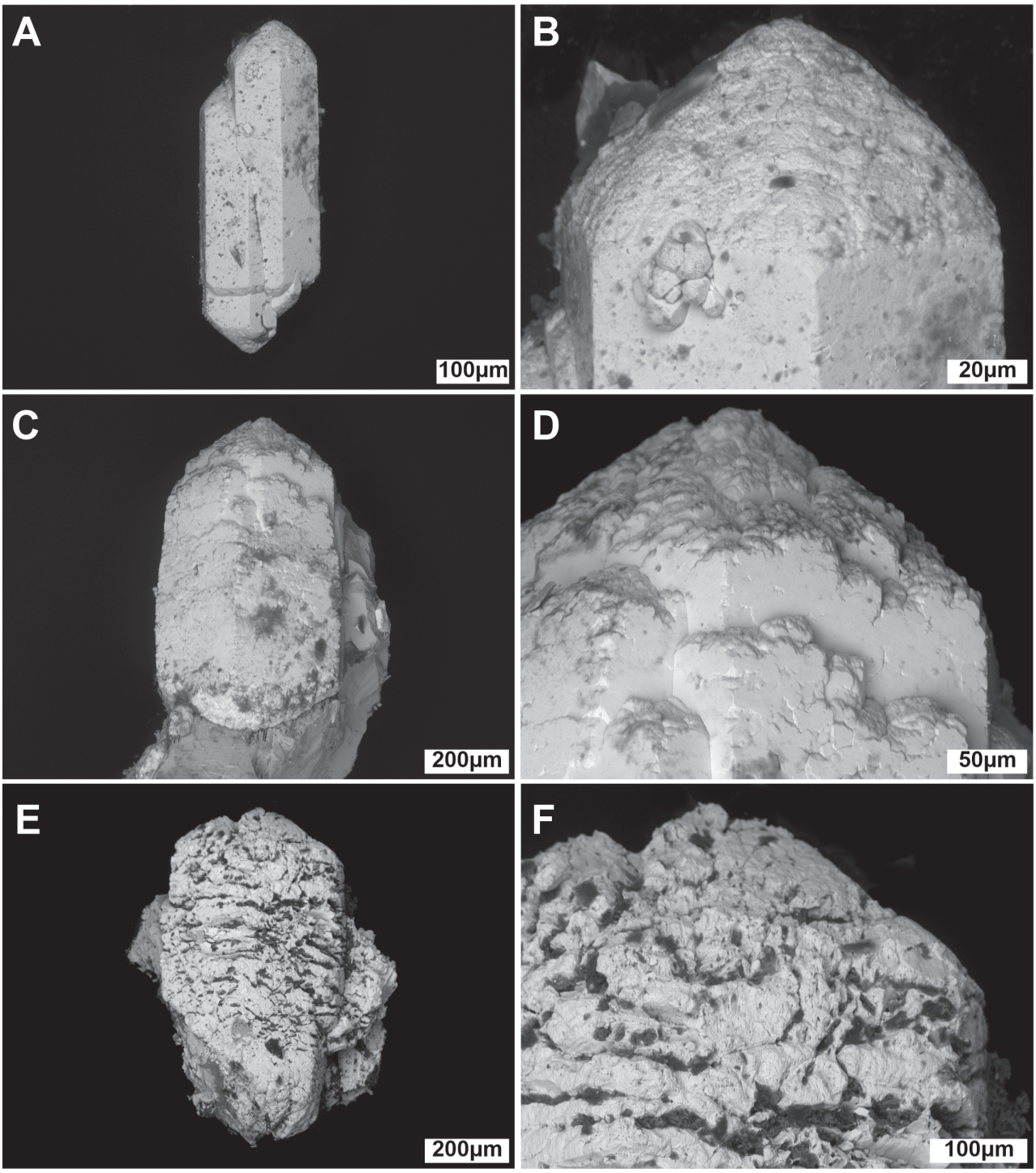

Figure 1. SEM images of three morphological varieties of double-terminated mimetite crystals from the quartz-baryte vein in Grodziszcze. Images B, D, and F are close-ups of pyramidal faces of respective crystals A, C, and E.

optical fibre with a diameter of 3.5 µm. An air Zeiss (LD EC Epiplan-Neofluan DIC-100/0.75NA) objective was used. Raman scattered light was focused by an effective Pinhole size of about 30 µm and a monochromator with a 600 mm^{-1} grating. The power of the laser at the sample position was 42 mW. Integration times of 10 s with an accumulation of 15 scans were chosen and a resolution of 3 cm^{-1}. Spectra processing was performed using the Spectracalc software package GRAMS (Galactic Industries Corporation, NH, USA). The Raman bands were fitted using a Gauss-Lorentz cross-product function with the minimum number of component bands used for the fitting process.

3. Results

3.1. Mimetite

Three morphologically different types of mimetite crystals have been observed: (I) well developed, yellow and transparent hexagonal prismatic crystals double terminated by bipyramids (Fig. 1A); (II) barrel-shaped, dark grey and opaque prismatic crystals with rough surface and dull appearance (Fig. 1C); (III) poorly-developed white prismatic crystals with etched faces (Fig. 1E). Type-I crystals show smooth prismatic faces and rough bipyramidal faces (Fig. 1A,B). Type-II crystals under SEM show features

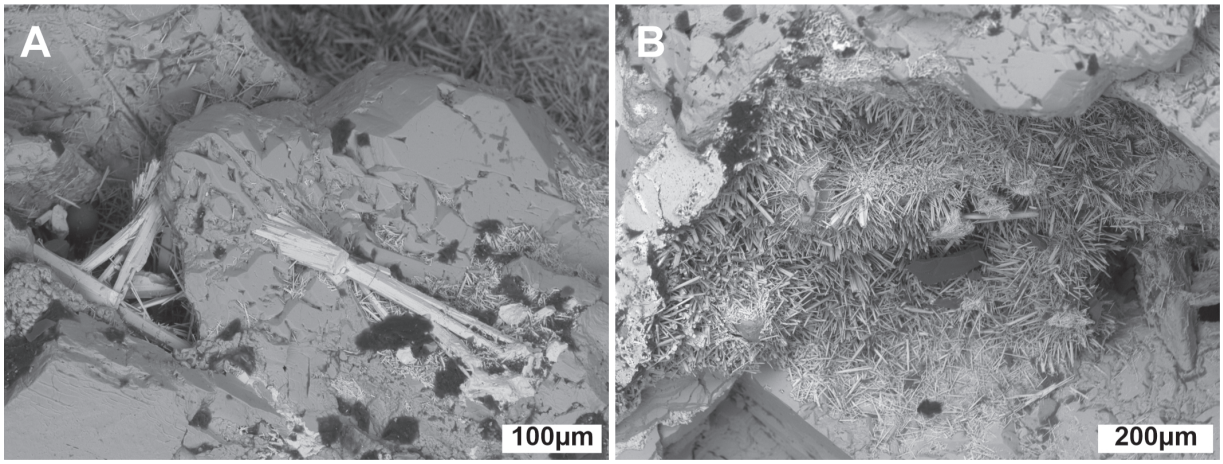

Figure 2. SEM images of pyromorphite from the quartz-baryte vein in Grodziszcze: (A) bundles of prismatic split-crystals on baryte; (B) aggregates of acicular crystals lining a cavity within baryte.

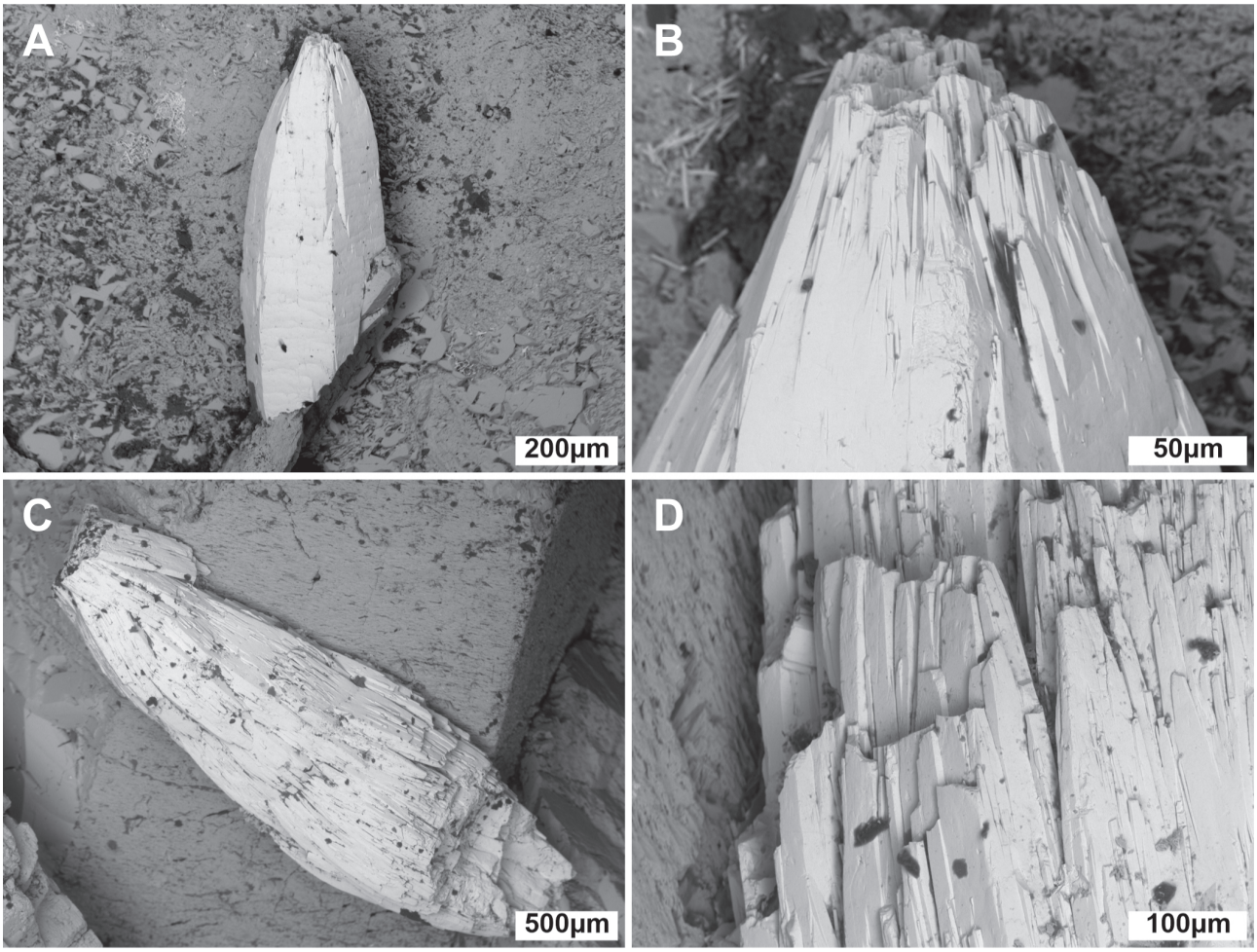

Figure 3. SEM images of apparent vanadinite crystals from the quartz-baryte vein in Grodziszcze: (A) barrel-shaped crystal on baryte; (B) close-up of the tip of the crystal shown in (A); (C) another split-crystal of apparent vanadinite; (D) details of the sub-individuals of the crystal shown in (C).

indicative of autoepitaxial overgrowths (Fig. 1C,D). All crystal faces of the type-III crystals are rough and porous with features typical of etching (Fig. 1E,F).

Type-I crystals appear homogeneous in reflected light under the optical microscope; whereas, type-II crystals are oscillatory zoned. Type-III crystals show sector zoning, whereas, oscillatory zoning is faintly expressed. Back-scattered electrons revealed zoning in apparently homogenous type-I crystals and confirmed oscillatory zoning in type-II crystals and sectorial zoning in type-III crystals.

Electron microprobe data for all three types of mimetite crystals are given in Table 1. Despite zoning, the P/As in the type-I crystal is low and uniform throughout the crystal, ranging from 0.01 to 0.02 (1.4 mol% of pyromorphite component) except for the

Table 1. EPMA data for three types of mimetite crystals from Grodziszcze.

	Crystal I				Crystal II			Crystal III	
	interior	rim			interior	rim		sectors:	
	Average* n = 4	1	2	3	Average* n = 5	1	2	1 n = 2	2 n = 2
	wt%								
SiO_2	0.07	0.11	0.22	0.27	0.21	0.22	0.13	0.20	0.25
	(*0.03-0.10*)				(*0.13-0.29*)				
Bi_2O_3	0.35	0.23	0.37	0.14	0.39	0.27	0.28	0.27	0.23
	(*0.28-0.46*)				(*0.19-0.67*)				
PbO	73.04	74.30	73.13	74.37	73.36	74.56	73.62	73.34	74.08
	(*72.31-73.54*)				(*72.67-73.56*)				
CaO	0.08	0.34	0.41	0.24	0.21	0.27	0.77	0.38	0.21
	(*0.04-0.18*)				(*0.13-0.29*)				
P_2O_5	0.19	1.62	2.24	3.26	0.93	1.40	2.04	1.67	1.08
	(*0.13-0.24*)				(*0.82-1.02*)				
As_2O_5	22.13	20.17	19.08	17.39	21.13	20.23	19.82	20.31	20.83
	(*21.91-22.33*)				(*20.98-21.4*)				
V_2O_5	0.02	0.06	0.06	0.10	0.02	0.00	0.00	0.01	0.04
	(*0.00-0.08*)				(*0.00-0.08*)				
SO_3	0.06	0.05	0.15	0.15	0.07	0.05	0.05	0.09	0.04
	(*0.01-0.12*)				(*0.01-0.14*)				
Cl	2.28	2.20	2.32	2.28	2.23	2.19	2.24	2.19	2.21
	(*2.22-2.30*)				(*2.20-2.25*)				
H_2O^c	0.02	0.05	0.02	0.03	0.04	0.05	0.05	0.06	0.04
Total	98.24	99.13	98.00	98.23	98.59	99.24	99.00	98.52	99.01
2Cl=O	0.51	0.50	0.52	0.51	0.50	0.49	0.51	0.49	0.50
Total^c	97.73	98.63	97.48	97.72	98.09	98.75	98.49	98.03	98.51
	apfu based on 12.5 anions								
Bi	0.023	0.015	0.023	0.009	0.025	0.027	0.018	0.017	0.015
Pb	4.963	4.933	4.842	4.913	4.911	4.977	4.824	4.843	4.944
Ca	0.022	0.090	0.108	0.063	0.043	0.069	0.201	0.100	0.056
Σ	5.008	5.038	4.973	4.985	4.978	5.063	5.043	4.960	5.014
P	0.041	0.338	0.466	0.677	0.196	0.294	0.420	0.347	0.227
As	2.921	2.601	2.453	2.231	2.747	2.623	2.523	2.605	2.700
V	0.003	0.010	0.010	0.010	0.003	0.000	0.000	0.002	0.007
Si	0.018	0.027	0.054	0.066	0.052	0.055	0.032	0.098	0.062
S	0.011	0.009	0.028	0.028	0.013	0.009	0.009	0.017	0.007
Σ	2.994	2.986	3.011	3.012	3.011	2.980	2.984	3.019	3.003
Cl	0.975	0.920	0.967	0.948	0.940	0.920	0.924	0.910	0.928
OH^c	0.025	0.080	0.033	0.052	0.060	0.080	0.076	0.090	0.072
Pym	1	12	16	23	7	10	14	12	8
Mim	99	88	84	77	93	90	86	88	92
Vna	0	0	0	0	0	-	-	0	0

*range of values is in brackets; H_2O^c and OH^c – calculated; Total^c – total corrected for Cl.

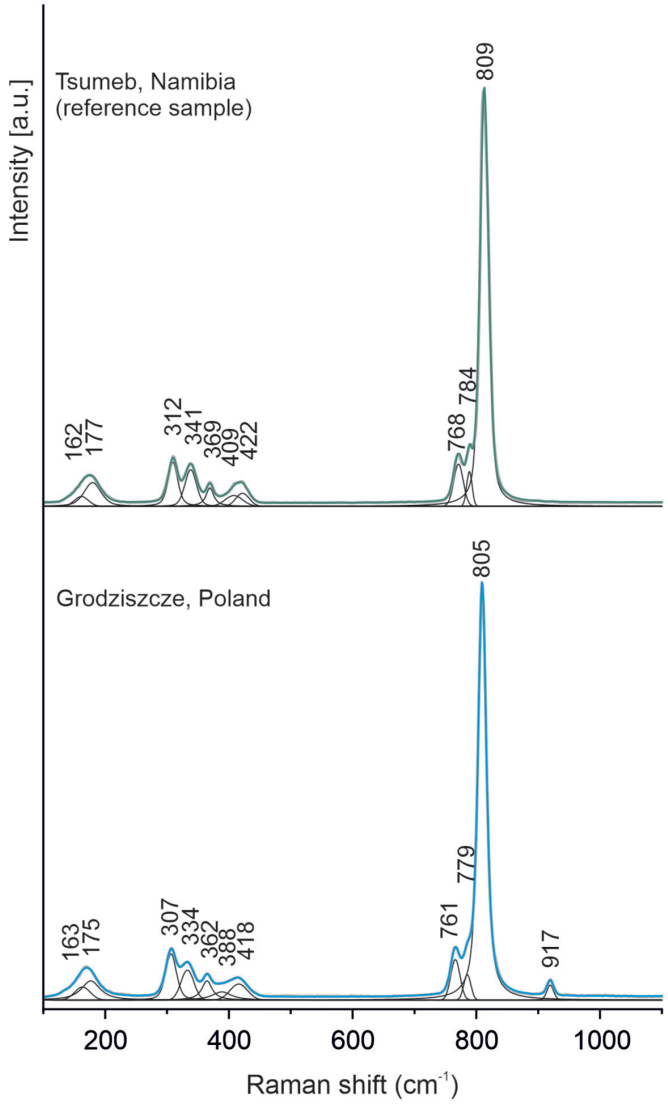

Figure 4. Raman spectra of mimetite from Tsumeb (Namibia) and Grodziszcze.

sharp increase in P within the 15 µm-wide outermost rim with the pyromorphite molecule ranging from 11.5 to 23.2 mol% (Table 1, analyses 1-3), i.e. an order of magnitude higher than in the interior of the crystal. The type-II mimetite crystal has slightly higher overall content of P compared to the type-I crystal (Table 1); however, likewise the type-I crystal, the mole fraction of pyromorphite is rather uniform throughout the crystal ranging from 6 to 7 mol% and increases sharply to 14.3 mol% in the outermost rim. In the type-III crystal, pyramidal sectors are slightly enriched in pyromorphite molecule (ca. 12 mol%) compared to prismatic sectors (ca. 8 mol%) (Table 1). In all of the types, V has either been undetected by EPMA or it is at most 0.01 apfu.

Raman spectrum of the mimetite type I crystal (Fig. 4) is characterised by very strong band at 805 cm^{-1} and two shoulder bands at 761 and 779 cm^{-1}, which, according to Frost et al. (2007) can be related to the ν_1 symmetric and ν_3 asymmetric stretching vibrations of $(AsO_4)^{3-}$. The lack of OH is in accord with EPMA data (Table 2) and is further confirmed by the absence of OH vibration bands in the Raman spectrum (the Raman spectrum above 3000 cm^{-1} is featureless and as such is not reproduced in Fig. 4). Bending vibrations are observed in the range of 300-430 cm^{-1}. Two bands at 307 and 334 cm^{-1} are assigned to ν_2 symmetric bending vibrations of $(AsO_4)^{3-}$. Bands at 362, 388, and 418 cm^{-1} are ascribed to the ν_4 asymmetric bending $(AsO_4)^{3-}$ vibrations. Bands below 200 cm^{-1} are assigned to the lattice modes.

The Raman spectrum of mimetite from Grodziszcze was compared to that of mimetite from Tsumeb, Namibia (a reference sample) (Fig. 4). The band at 917 cm^{-1} seen in the Raman spectrum of mimetite from Grodziszcze is absent in the Tsumeb sample. That band is assigned to the ν_1 symmetric stretching mode of $(PO_4)^{3-}$ resulting from the phosphate anions substitution for arsenate anions in mimetite (Bajda et al., 2011) in accord with the EPMA data for the outermost zones in the investigated mimetite (Table 1).

3.2. Pyromorphite-mimetite-vanadinite single crystal

The investigated polymineralic crystal is built up of alternating mimetite, pyromorphite, and vanadinite zones as revealed by BSE imaging (Fig. 5), X-ray elemental maps (Fig. 6), and EPMA data (Table 2).

Cross-section of the crystal along *c*-axis shows complex pattern of zonation and overgrowths of multigeneration PyGM (Figs. 5 and 6): (a) pyromorphite + vanadinite porous and oscillatory-zoned core (Pym I + Vna I), (b) narrow band of pyromorphite (Pym II), (c) two mimetite zones (Mim I and Mim II) intercalated by a thin band of pyromorphite and vanadinite (Pym III + Vna II), and (d) vanadinite mantle (Vna III).

The core (Pym I + Vna I) consists of predominant pyromorphite alternating with narrow (<2 µm thick) zones of vanadinite. Acicular crystals of pyromorphite are aligned along the longer axis of the crystal. The curved shape of the zones seen in Figs. 5 and 6 resulted from the split crystal growth. Outer portions of the core are enriched in V (analyses 3 to 5 in Table 2). The distribution of As in the core is random and patchy (Fig. 6). EPMA data were obtained with the electron beam of ca. 5 µm diameter. Therefore, elevated concentrations of V in analyses of the pyromorphite zones (analyses 3 and 4 in Table 2) may have resulted from the contaminations from the adjacent vanadinite zones rather than from the extended pyromorphite-vanadinite solid solution.

The Pym II zone is poorly preserved and highly fractured, which precluded reliable EPM analyses. Pyromorphite was identified based on X-ray elemental maps (Table 1) and EDS spectra (not shown here).

The intermediate portion of the crystal consists of the first generation mimetite (Mim I in Fig. 5) overgrown by alternating pyromorphite-vanadinite narrow zone (Pym III + Vna II). Mimetite I precipitated preferentially on the bipyramidal sectors of the growing crystals. Second generation mimetite (Mim II) continued to preferentially

Table. 2. EPMA data for three regions within the polymineral mimetite-pyromorphite-vanadinite crystal shown in Fig. 5.

Regions	core					intermediate				
Spots:	1 PymI +VnaI	2 PymI +VnaI	3 PymI +VnaI	4 PymI +VnaI	5 PymI +VnaI	6 MimI	7 MimI	8 MimI	9 MimI	10 PymIII
					wt%					
SiO_2	0.04	0.06	0.08	0.11	0.22	0.13	0.09	0.19	0.31	0.04
Bi_2O_3	0.23	0.49	0.42	0.46	0.31	0.46	0.30	0.42	0.20	0.29
PbO	79.60	78.58	77.71	79.09	75.97	73.67	74.64	74.13	72.47	78.89
CaO	0.13	0.56	0.26	0.23	0.17	0.13	0.14	0.12	0.53	0.34
FeO	0.00	0.00	0.00	0.00	0.13	0.00	0.10	0.07	0.00	0.00
ZnO	0.00	0.00	0.14	0.00	0.00	0.11	0.00	0.07	0.00	0.00
P_2O_5	14.23	13.78	12.20	10.40	1.13	0.88	1.52	0.72	1.34	14.13
As_2O_5	1.44	1.40	1.91	2.42	4.37	20.97	19.88	20.98	20.61	1.32
V_2O_5	0.11	0.36	2.27	4.01	13.65	0.00	0.07	0.00	0.00	0.00
SO_3	0.09	0.05	0.17	0.09	0.16	0.00	0.00	0.06	0.08	0.03
Cl	2.39	2.35	2.36	2.33	2.11	2.31	2.26	2.26	2.20	2.32
H_2O^c	0.04	0.05	0.05	0.06	0.09	0.01	0.02	0.02	0.05	0.05
Total	98.30	97.68	97.57	99.20	98.31	98.67	99.02	99.04	97.79	97.41
2Cl = O	0.54	0.53	0.53	0.53	0.48	0.52	0.51	0.51	0.50	0.52
$Total^{cor}$	97.76	97.15	97.04	98.67	97.83	98.15	98.51	98.53	97.29	96.89
					apfu based on 12.5 anions					
Bi	0.02	0.04	0.04	0.03	0.03	0.04	0.03	0.04	0.02	0.03
Pb	4.95	4.92	4.84	4.93	4.89	4.98	5.03	5.01	4.81	4.96
Ca	0.03	0.14	0.06	0.06	0.04	0.03	0.04	0.03	0.14	0.09
Fe	0.00	0.00	0.00	0.00	0.03	0.00	0.02	0.01	0.00	0.00
Zn	0.00	0.00	0.02	0.00	0.00	0.02	0.00	0.01	0.00	0.00
Σ	5.00	5.07	5.00	5.05	4.99	5.07	5.12	5.10	5.21	5.28
P	2.78	2.71	2.39	2.04	0.23	0.19	0.32	0.15	0.28	2.80
As	0.17	0.17	0.23	0.29	0.55	2.75	2.60	2.75	2.66	0.16
V	0.02	0.06	0.35	0.61	2.16	0.00	0.01	0.00	0.00	0.00
Si	0.01	0.01	0.02	0.03	0.05	0.03	0.02	0.05	0.08	0.01
S	0.02	0.01	0.03	0.02	0.03	0.00	0.00	0.01	0.01	0.01
Σ	3.00	2.94	3.01	2.96	3.02	2.97	2.91	2.96	3.19	3.10
Cl	0.94	0.93	0.93	0.91	0.85	0.98	0.96	0.96	0.92	0.92
OH^c	0.06	0.08	0.07	0.09	0.15	0.02	0.04	0.04	0.08	0.08
Pym	94	92	80	69	8	6.5	11	5	9.5	95
Mim	6	6	8	10	19	93.5	89	95	90.5	5
Vna	0	2	12	21	73	0	0	0	0	0

Regions	intermediate					outermost				
Spots:	11 MimII	12 MimII	13 MimII	14 VnaIII	15 VnaIII	16 VnaIII	17 VnaIII	18 VnaIII	19 VnaIII	20 VnaIII
SiO_2	0.09	0.07	0.01	0.14	0.17	0.26	0.32	0.28	0.38	0.43
Bi_2O_3	0.36	0.17	0.37	0.39	0.43	0.37	0.32	0.15	0.52	0.29
PbO	73.53	75.15	73.98	75.41	75.67	76.00	76.39	76.94	75.39	75.46
CaO	0.57	0.21	0.21	0.04	0.03	0.05	0.01	0.03	0.10	0.05
FeO	0.00	0.04	0.16	0.11	0.00	0.00	0.01	0.00	0.05	0.18
ZnO	0.00	0.08	0.16	0.00	0.00	0.00	0.01	0.00	0.05	0.18
P_2O_5	1.40	2.09	1.59	0.37	0.26	0.31	0.20	0.21	0.70	0.49

(*Continued*)

Table. 2. Continued

Regions	intermediate					outermost				
Spots:	11 MimII	12 MimII	13 MimII	14 VnaIII	15 VnaIII	16 VnaIII	17 VnaIII	18 VnaIII	19 VnaIII	20 VnaIII
As_2O_5	20.59	19.49	20.25	1.38	0.93	1.31	0.55	0.58	3.10	1.58
V_2O_5	0.11	0.05	0.08	19.46	19.11	18.99	20.09	19.46	16.81	17.54
SO_3	0.14	0.09	0.07	0.07	0.03	0.08	0.05	0.15	0.03	0.02
Cl	2.18	2.32	2.03	2.21	2.17	2.27	2.22	2.15	2.15	2.15
H_2O^c	0.06	0.02	0.09	0.11	0.10	0.09	0.11	0.11	0.11	0.10
Total	99.03	99.78	99.00	99.69	98.90	99.73	100.28	100.06	99.39	98.37
2Cl = O	0.49	0.52	0.46	0.50	0.49	0.51	0.49	0.49	0.49	0.49
$Total^{cor}$	98.54	99.26	98.54	99.19	98.41	99.22	99.79	99.57	98.90	97.88
apfu based on 12.5 anions										
Bi	0.03	0.02	0.03	0.03	0.04	0.03	0.03	0.01	0.05	0.03
Pb	4.84	4.96	4.91	4.55	4.69	4.64	4.61	4.70	4.63	4.72
Ca	0.15	0.06	0.06	0.01	0.01	0.01	0.00	0.01	0.02	0.01
Fe	0.00	0.01	0.03	0.02	0.00	0.00	0.00	0.00	0.01	0.04
Zn	0.00	0.01	0.03	0.00	0.00	0.00	0.00	0.00	0.01	0.03
Σ	4.87	5.06	5.06	4.61	4.74	4.68	4.64	4.72	4.72	4.83
P	0.29	0.43	0.33	0.07	0.05	0.06	0.04	0.04	0.14	0.10
As	2.63	2.50	2.61	0.16	0.11	0.16	0.06	0.07	0.37	0.19
V	0.02	0.01	0.01	2.88	2.91	2.85	2.97	2.92	2.53	2.70
Si	0.02	0.02	0.00	0.03	0.04	0.06	0.07	0.06	0.09	0.10
S	0.03	0.02	0.01	0.01	0.01	0.01	0.01	0.04	0.01	0.00
Σ	2.99	2.98	2.96	3.15	3.12	3.14	3.15	3.13	3.14	3.09
Cl	0.90	0.96	0.85	0.84	0.85	0.87	0.84	0.83	0.83	0.85
OH^c	0.10	0.04	0.15	0.16	0.15	0.13	0.16	0.17	0.17	0.15
Pym	15	15	11	2	2	2	1	1.3	5	3
Mim	85	85	89	5	3	5	2	2.3	12	7
Vna	0	0	0	93	95	93	97	96.4	83	90

H_2O^c and OH^c – calculated; $Total^{cor}$ – total corrected for Cl.

grow on bipyramidal faces. Mimetites I and II lack vanadinite component. The content of pyromorphite molecule in mimetite ranges from 5 to 15% (Table 2).

The outermost portions of the crystal (Vna III) consists of almost pure vanadinite (83 – 97 mol%) (analyses 14-18 and 20 in Table 2). The Raman spectrum of the vanadinite overgrowth (Fig. 7) is featured by sharp and intense band at 823 cm^{-1}, which, according to Frost et al. (2003), results the ν_1 symmetric stretching vibrations of $(VO_4)^{3-}$ (Fig. 7). Shoulder bands at 789 and 726 cm^{-1} are related to the ν_3 asymmetric stretching vibrations of $(VO_4)^{3-}$. Bending vibrations are observed in the spectral range 280-420 cm^{-1}. Two Raman bands at 316 and 343 cm^{-1} are ascribed to the ν_2 symmetric bending O-V-O vibrations, while band at 408 cm^{-1} is correlated with the ν_4 asymmetric bending O-V-O vibrations. Band below 200 cm^{-1} are assigned to the lattice modes. The Raman spectrum of the vanadinite overgrowth is similar to the reference vanadinite from Mibladen, Morocco (Fig. 7).

The distribution of Pb and Bi is uniform throughout the crystal varying within 0.27 apfu with only insignificant substitution of Pb by Ca (Table 2). The Ca/Pb ratio does not exceed 0.03.

X-ray elemental maps reveal sharp boundaries between compositionally contrasting zones (Fig. 6). Each zone represents a single mineral with limited solid solution as suggested by EPMA. In mimetite zones, the substitution of As by P does not exceed 0.43 apfu. Vanadinite is even purer, with As + P = 0.30 apfu, at most. The EPMA data show limited miscibility between all three minerals in a composite crystal (Fig. 8). The maximum extent of solid solutions is not larger than 30 mol%. Most analyzes, however, cluster around 10 mol% of solid solution.

4. Discussion

The occurrence of three morphological types of mimetite crystals observed in this study can be explained by different crystal growth mechanisms. Well-developed crystals (Fig. 1A) most probably crystallized slowly at relatively low supersaturation of aqueous solution. Crystals built up of sub-parallel individuals

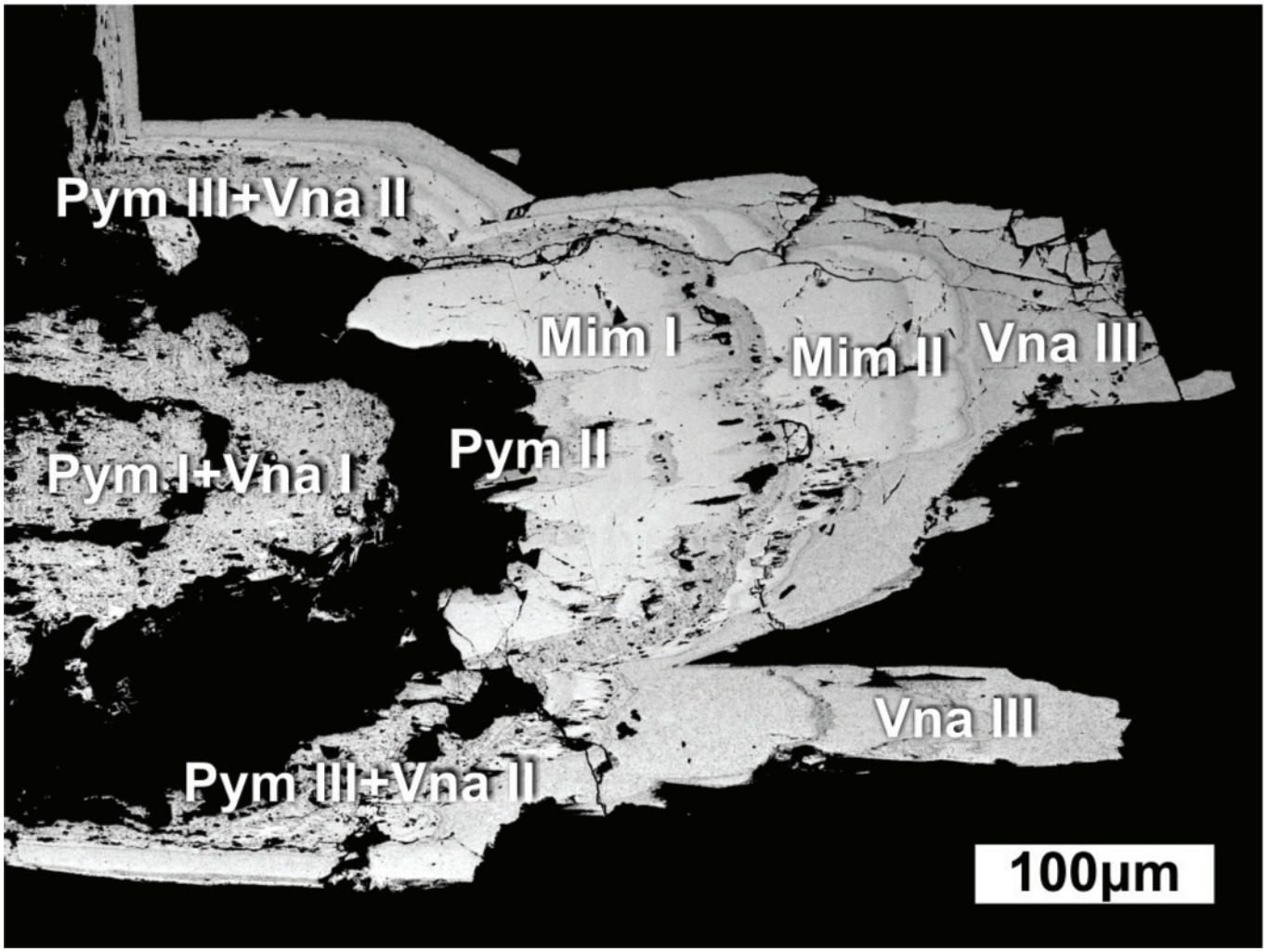

Figure 5. BSE image of vanadinite-mimetite-pyromorphite crystal. Mim – mimetite, Pym – pyromorphite, Vna – vanadinite.

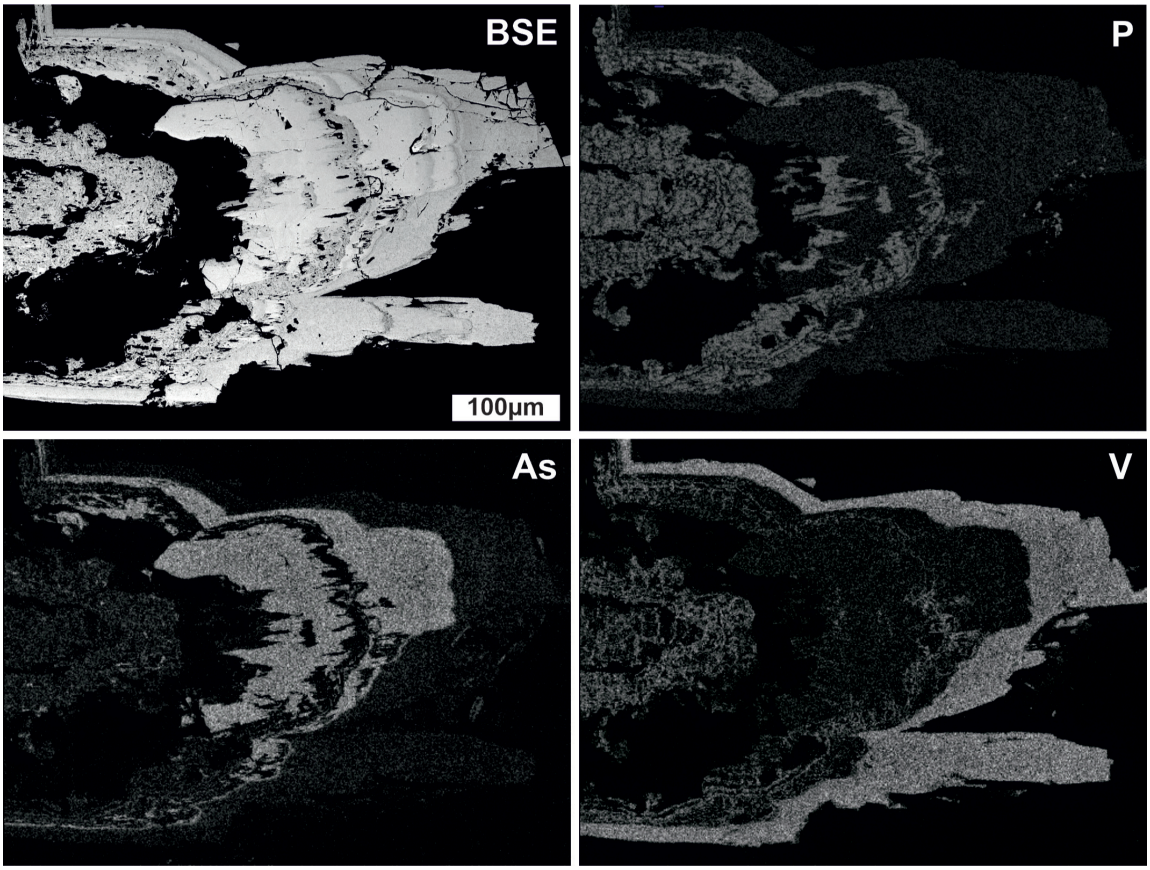

Figure 6. BSE image and X-ray elemental maps of As – Arsenic, V – Vanadium, and P – Phosphorus.

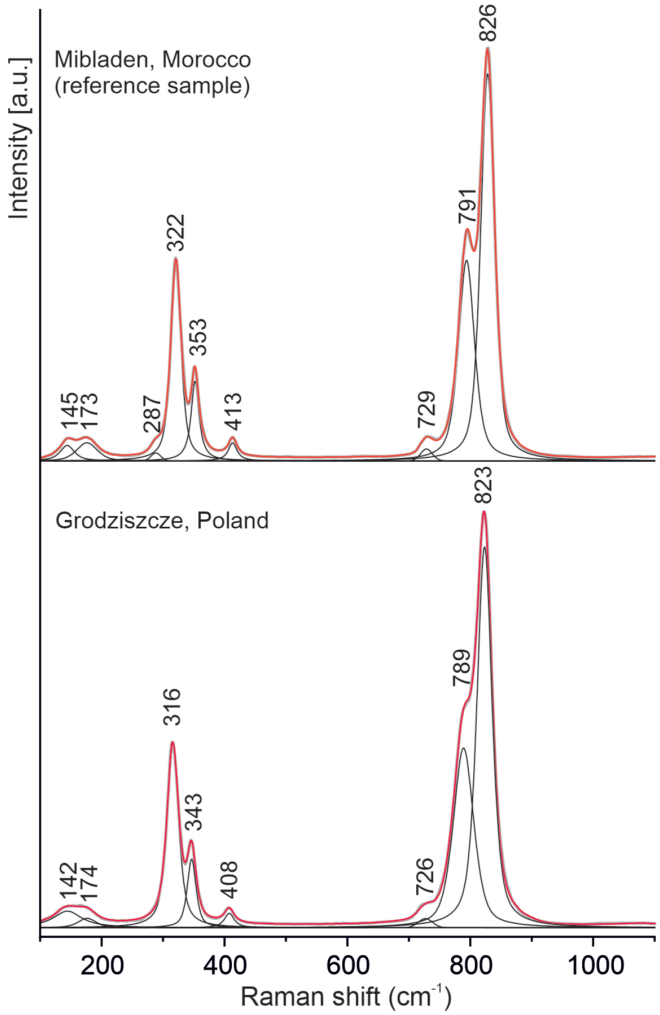

Figure 7. Raman spectra of vanadinite from Mibladen (Morocco) and Grodziszcze.

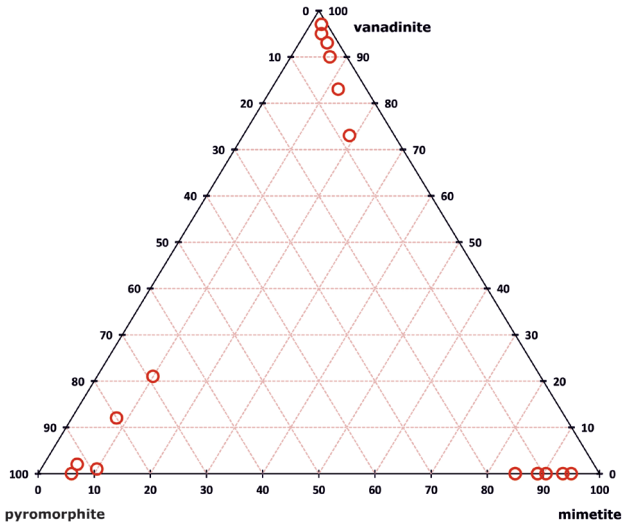

Figure 8. Ternary plot for mimetite-pyromorphite-vanadinite zones and overgrowths in the polymineralic crystal.

(Fig. 1C) are good examples of autoepitaxial growth by parallel accretion (Kostov & Kostov, 1999). The third type crystals also grew by parallel accretion; however, it was etched significantly. As a result of etching, the crystal faces are rough and undeveloped. The cause for the etching is unclear. The co-occurrence of the PyGM crystals and cerussite suggests near-neutral to alkaline pH of aqueous solution from which those minerals crystallized (Keim & Markl, 2015). Possibly, decrease in the solution pH may have caused partial dissolution of the mimetite crystal.

The occurrence of different types of mimetite crystals in different samples from the same quartz-baryte vein suggests localized different crystal-growth conditions, i.e. the degree of supersaturation, changes in the solution pH and activity of $(PO_4)^{3-}$. The most peculiar conditions of crystal growth occurred in a site of the crystallization of polymineralic crystals.

The temporal sequence of crystallization within the polymineralic crystal inferred from BSE images and X-ray elemental maps (Figs. 5 and 6) can be summarized as follows: {oscillatory-zoned core built up of pyromorphite I and subordinate vanadinite I} → {pyromorphite II} → {mimetite I} → {oscillatory banded pyromorphite III and minor vanadinite II} → {mimetite II} → {vanadinite III}.

Markl et al. (2014) explained zoning in PyGM crystals as a result of single episodes of fluid flow. Each homogeneous zone reflects a period of fluid influx. However, the oscillatory zoning observed in the core and in the intercalation between mimetites I and II, can alternatively be explained by the relative changes in P and V ions concentrations at the crystal/solution interface, i.e. within the diffusion boundary layer, in accord with the models of the autocatalytic crystal growth in binary solid solutions (Sánchez-Pastor et al., 2005 and references therein). According to these models, crystallization of one end-member of the solid solution results in the depletion in that component of the adjacent aqueous solution and the precipitation of the second end-member with cyclic repetition of that process (ibid.).

The polymineralic crystals are built of parallelly oriented subindividuals (Fig. 3), which is a feature indicative of split growth due to high growths rates (Sunagawa, 2007). As the crystal front moves fast, there is not enough time for the re-equilibration within the diffusion boundary layer. Precipitation of pyromorphite from the supersaturated aqueous solution may have caused the depletion of the boundary layer in P, while the concentration of V relatively increased until it reached the threshold supersaturation for the crystallization of vanadinite. The oscillatory precipitation of pyromorphite and vanadinite in the crystal core proceeded until the exhaustion of solutes and was repeated after the crystallization of mimetite I. The concentration of P may not have been high, because even small amount of P in aqueous solutions promotes the precipitation of pyromorphite-rich solids (Flis et al., 2011).

The formation of the two wide mimetite zones (Figs. 5 and 6) may have resulted either from the relative enrichment in aqueous As or due to inflow of As-rich solution interrupted by the precipitation of pyromorphite II. Mimetite crystals are the most abundant of PyGM in

the quartz-baryte vein; however, they have not been observed in the proximity of the polymineralic crystals. Therefore, it is not clear, whether the formation of both mimetite zones in polymineralic crystals temporarily coincided with the formation of mimetite crystals elsewhere in the vein. EPMA data for mimetite zones (Table 2) and for mimetite crystals are similar (Table 1), though the latter are slightly enriched in pyromorphite molecule.

Exhaustion of As and P in the solution resulted in the relative enrichment in V ions and subsequent epitaxial overgrowth of the pyromorphite/mimetite crystals by almost pure vanadinite. Most probably, the conditions favorable for the formation of polymineralic crystals, including high concentration of aqueous V, were localized.

5. Conclusions

All of the observed different PyGM crystals are spatially separated, which suggests localized conditions within the quartz-baryte vein, suitable for their crystallization rather than uniform crystallization front. The aqueous solution differed locally in activities of $(AsO_4)^{-3}$, $(PO_4)^{-3}$, and $(VO_4)^{-3}$; whereas, the overall activities of Pb^{2+} and Cl^- were high. Locally, the activities of all anions were sufficiently high for the crystallization of polymineralic crystals composed of all three PyGM. The co-occurrence of cerussite is indicative of near neutral or slightly alkaline pH during the crystallization of PyGM with possible local decrease in pH as suggested by the occurrence of the etched mimetite crystals.

While there is a continuous ternary solid solution among the PyGM, the present study suggests that kinetically driven growth of PyGM crystals may result in precipitation of discrete mineral phases with limited anionic substitutions due to autocatalytic mechanism. There might be no new fluid fluxes involved in the precipitation of homogeneous zones or overgrowths to crystallize polymineralic crystals. Instead, those zones and overgrowths may have originated due to changes in the relative concentrations of elements within the diffusion boundary layer at the crystal/solution interface during the crystal growth.

Acknowledgment

We are grateful to Bartosz Puzio and anonymous reviewers for their critical comments, which significantly improved the final version of this article. This study was financially supported by a statutory fund of the Institute of Earth Sciences, Faculty of Natural Sciences, University of Silesia in Katowice, which we gratefully acknowledge.

Statement about the conflicts of interest

There are no conflicts of interest.

References

Bajda, T., Mozgawa W., Manecki M., & Flis, J. (2011). Vibrational spectroscopic study of mimetite–pyromorphite solid solutions. *Polyhedron*, *30*, 2479–2485. https://doi.org/10.1016/j.poly.2011.06.034

Breemen, O., van, Bowes, D. R., Aftalion, M., & Żelaźniewicz, A. (1988). Devonian tectonothermal activity in the Sowie Góry gneissic block, Sudetes, southwestern Poland: evidence from Rb-Sr and U-Pb isotopic studies. *Annales Societatis Geologorum Poloniae 58*, 3–19.

Flis, J., Manecki, M., & Bajda, T. (2011). Solubility of pyromorphite $Pb_5(PO_4)_3Cl$ – mimetite $Pb_5(AsO_4)_3Cl$ solid solution series. *Geochimica et Cosmochimica Acta 75(7)*, 1858–1868. https://doi.org/10.1016/j.gca.2011.01.021

Frost, R.L., Bouzaid, J.M., Palmer, S. (2007). The structure of mimetite, arsenian pyromorphite and hedyphane – A Raman spectroscopic study. *Polyhedron*, *26*, 2964–2970. https://doi.org/10.1016/j.poly.2007.01.038

Frost, R.L., Crane, M., Williams, P.A., & Kloprogge, J.T. (2003). Isomorphic substitution in vanadinite $[Pb_5(VO_4)_3Cl]$ – a Raman spectroscopic study. *Journal of Raman Spectroscopy 34(3)*, 214–220. https://doi.org/10.1002/jrs.978

Inegbenebor, A.I., Thomas, J.H., & Williams, P.A. (1989). The chemical stability of mimetite and distribution coefficients for pyromorphite-mimetite solid solutions. *Mineralogical Magazine 53*, 363–371.

Janicka, U., Bajda, T., Topolska, J., & Manecki, M. (2014). Optimization of synthesis conditions of pyromorphite-vanadynite and mimetite-vanadynite solid solution series. *Geology, Geophysics and Environment 40(1)*, 88–88.

Jastrzębski, M., Budzyń, B., Żelaźniewicz, A., Konečný, P., Sláma, J., Kozub-Budzyń, G. A., Skrzypek, E., & Jaźwa, A. (2021). Eo-Variscan metamorphism in the Bohemian Massif: Thermodynamic modelling and monazite geochronology of gneisses and granulites of the Góry Sowie Massif, SW Poland. *Journal of Metamorphic Geology*, *39(6)*, 751–779.

Keim, M.F., & Markl, G. (2015). Weathering of galena: Mineralogical processes, hydrothermal fluid path modeling, and estimation of the growth rate of pyromorphite. *American Mineralogist 100(7)*, 1584–1594. https://doi.org/10.2138/am-2015-5183

Keper, J.C. (2004). The Goodsprings mining district, Clark County. In: Minerals of Nevada (S.B. Castor, G.C. Ferdock, eds.) Nevada Bureau of Mines and Geology Special Publications. p 91–101.

Ketcham, R.A. (2015). Calculation of stoichiometry from EMP data for apatite and other phases with mixing on monovalent anion sites. *American Mineralogist 100(7)*, 1600–1623. https://doi.org/10.2138/am-2015-5171

Kostov, I., & Kostov, R. (1999). Crystal habits of minerals. Prof. Marin Drinov Publishing House & Pensoft Publishers, Sofia.

Markl, G., Marks, M.A.W., Holzäpfel, J., & Wenzel, T. (2014). Major, minor, and trace element composition of pyromorphite-group minerals as recorder of supergene weathering processes from the Schwartzwald mining district, SW Germany. *American Mineralogist 99(5-6)*, 1133–1146. https://doi.org/10.2138/am.2014.4789

Nakamoto, A., Urasima, Y., Sugura, S., Nakano, H., Yachi, T., & Tadokoro, K. (1969). Pyromorphite-mimetite minerals

from the Otaru-Matsukura baryte mine in Hokkaido, Japan. *Mineralogical Journal 6(1/2)*, 85–101.

Pasero, M., Kampf, A.R., Ferraris, C., Pekov, I.V., Rakovan, J., & White, T.J. (2010). Nomenclature of the apatite supergroup minerals. *European Journal of Mineralogy 22(2)*, 163–197. https://doi.org/10.1127/0935-1221/2010/0022-2022

Puzio, B., Solecka, U., Topolska, J., Manecki, M., & Bajda, T. (2021). Solubility and dissolution mechanisms of vanadinite $Pb_5(VO_4)_3Cl$: Effects of temperature and PO_4 substitutions. *Applied Geochemistry 131*, 105015. https://doi.org/10.1016/j.apgeochem.2021.105015

Sánchez-Pastor, N., Pina, C.M., Astilleros, J.M., Fernández-Díaz, L., & Putnis A. (2005). Epitaxial growth of celestite on baryte (001) face at a molecular scale. *Surface Science 581*, 225–235. https://doi.org/10.1016/j.susc.2005.02.051

Solecka, U., Bajda, T., Topolska, J., Zelek-Pogudz, S., & Manecki, M. (2018). Raman and Fourier transform infrared spectroscopic study of pyromorphite-vanadinite solid solutions. *Spectrochimica Acta A*. *190*, 96–103. https://doi.org/10.1016/j.saa.2017.08.061

Song, H., Liu, J., & Cheng, H. (2018). Structural and spectroscopic study of arsenate and vanadate incorporation into apatite group: implications for semi-quantitative estimation of As and V contents in apatite. *Spectrochimica Acta 188*, 488–494. https://doi.org/10.1016/j.saa.2017.07.028

Stysz, M. & Mączka, M. (2007). The Friedrich von Thielau mine in the Sowie Mts. *Sudety 10*. 8–9 (in Polish).

Sunagawa, I. (2007). Crystals. Growth, Morphology and Perfection. Cambridge University Press.

Szełęg, E. (2008). Vanadinite from Stanisław quarry (Izerskie Garby Zone, Sudetes, Poland). Mineralogia - Special Papers, 32.

Szełęg, E. (2023). Minerały i skały Polski. Multico Oficyna Wydawnicza, Warszawa.

Traube, H. (1888). Die Minerale Schlesiens. J.U. Kern's Verlag. Breslau.

Received: 07 Jan 2024
Accepted: 31 Jul 2024
Handling Editor: Tomasz Bajda